Available online at www.sciencedirect.com
SCIENCE DIRECT®
Journal of Computational Physics 192 (2003) 452–470
JOURNAL OF COMPUTATIONAL PHYSICS
www.elsevier.com/locate/jcp

A fully-implicit model of the global ocean circulation

Wilbert Weijer [a,1], Henk A. Dijkstra [a,*], Hakan Öksüzoğlu [b,2], Fred W. Wubs [b], Arie C. de Niet [b]

[a] *Institute for Marine and Atmospheric Research Utrecht, Department of Physics and Astronomy, Utrecht University, Utrecht, The Netherlands*
[b] *Research Institute for Mathematics and Computer Science, University of Groningen, Groningen, The Netherlands*

Received 25 November 2002; received in revised form 1 July 2003; accepted 16 July 2003

Abstract

With the recent developments in the solution methods for large-dimensional nonlinear algebraic systems, fully-implicit ocean circulation models are now becoming feasible. In this paper, the formulation of such a three-dimensional global ocean model is presented. With this implicit model, the sensitivity of steady states to parameters can be investigated efficiently using continuation methods. In addition, the implicit formulation allows for much larger time steps than can be used with explicit models. To demonstrate current capabilities of the implicit global ocean model, we use a relatively low-resolution (4° horizontally and 12 levels vertically) version. For this configuration, we present: (i) an explicit calculation of the bifurcation diagram associated with hysteresis behavior of the ocean circulation and (ii) the scaling behavior of the Atlantic meridional overturning versus the magnitude of the vertical mixing coefficient of heat and salt.

PACS: 65P30; 65N25; 76E20

Keywords: Stability of geophysical flows; Numerical bifurcation theory; Hysteresis behavior; Iterative linear systems solver

1. Introduction

The last decade has witnessed an enormous increase of interest in the dynamics of the ocean circulation to understand its role in the climate system [1]. On time scales of a decade to thousands of years, oceanic processes are a dominant factor in controlling the patterns and amplitude of climate variability. A typical

* Corresponding author. Tel.: +31-30-253-3858; fax: +31-30-254-3163.
E-mail address: dijkstra@phys.uu.nl (H.A. Dijkstra).
URL: http://www.phys.uu.nl/~dijkstra.
[1] Now at Scripps Institute of Oceanography, UCSD, La Jolla, CA, USA.
[2] Now at Institute for Marine and Atmospheric Research Utrecht.

0021-9991/$ - see front matter
doi:10.1016/j.jcp.2003.07.017

example is the interdecadal variability as observed in North Atlantic sea-surface temperature records [2,3] which is likely caused by changes in the thermohaline (i.e. density driven) ocean circulation [4].

As both the instrumental record of observations and the current paleodatabase is by far inadequate to assess the role of the ocean on these long time scales, there is an enormous effort to model the ocean circulation, both in isolation as well as coupled to the atmosphere and cryosphere. For studies of the variability of the ocean circulation on decades or less, high-resolution eddy-resolving models are used. Low-resolution models are typically used in climate related problems since long time intervals of integration can be achieved [5].

There are several models available which can be used to study the global ocean circulation. One of the well-known models is the Modular Ocean Model (MOM, [6]); a much used climate configuration has a horizontal and vertical resolution of 4° and 12 layers [7]. Other types of models are the Miami Isopycnal Ocean Model (MICOM, [8]) and the Hamburg Large-Scale Geostrophic (LSG) model [9]. While MOM and MICOM are fully explicit [10] and use time steps of typically one hour, the LSG model is semi-implicit and can run with time-steps up to one month.

A problem that has been much studied in the literature is the sensitivity of the global thermohaline circulation to anomalies in the freshwater flux. Many models have a parameter regime where multiple equilibria of the thermohaline circulation occur. A typical transient simulation demonstrating the existence of the multiple equilibria is a quasi-equilibrium run where the freshwater input is changed very slowly with respect to the equilibration time scale of the flow. The multiple equilibria show up as a hysteresis curve when the anomalous forcing is first increased and then decreased [7,11]. The jumps in the hysteresis curve are related to a transition from one stable state to another one.

Models such as MOM, MICOM and LSG are capable of forward time integration only and hence can only determine (linearly) stable states. However, in a typical bifurcation diagram associated with the hysteresis there are also unstable states [12]. While these states remain hidden for the forward models, they play an important role in the transient behavior of the flow, for example in the response to a temporary input of freshwater [13,14]. One would like to have models that determine these unstable equilibrium states directly and that are able to follow these states efficiently in parameter space.

It is here that there is a role for fully-implicit ocean models. The 'common knowledge' advantage of the formulation of these models is that the time step is not limited by numerical stability but by accuracy, the latter related to changes in the solution. On the other hand, the time steps are much more expensive because a system of nonlinear algebraic equations has to be solved within each time step. Whether the implicit model is computationally more efficient than an explicit model depends on a lot of factors and a comparison is in most cases difficult. However, when the linear systems solver performs well for large time steps, one is also able to compute solutions to the steady state equations directly. As the solver for the nonlinear equations determines isolated solutions, the steady states found may be either linearly stable or unstable. When an implicit model is combined with a parameter continuation, the steady states can be efficiently followed in parameter space.

When the Newton–Raphson method is used, several large-dimensional linear algebraic systems have to be solved. Each of these involve sparse nonsymmetric ill-conditioned and usually banded matrices. Direct solvers limit the dimension of these systems to several thousands. However, over the last decades a number of iterative solvers have been developed which enable one to tackle systems having dimensions up to a few hundred thousand; here application to global ocean models comes within reach.

A first step in the development of implicit ocean models was presented in [15]. For a single-hemispheric sector domain, it was shown that three-dimensional ocean flows could be computed using much larger time steps – in the approach to equilibrium, time steps of 50 years could be taken – than with explicit models. In addition, it was demonstrated that with the implicit formulation, steady states could be followed in parameter space without computing any transient behavior; this is efficient to determine parameter sensitivity of the flows. Finally, it was shown that the linear stability of steady states could be determined explicitly.

Although several limitations of the fully-implicit model were presented in [15], it was stated that the implicit approach would be applicable to a global ocean model with full continental geometry and bottom topography. In this paper, we present results computed with such a fully-implicit global ocean model using a relatively low horizontal resolution. Although there remain limitations with respect to representing the global ocean flow as it is observed today, the results shown here are a major step forward in the development of implicit ocean models. The advantages of the implicit approach are demonstrated by computing the sensitivity of the ocean circulation versus changes in the spatial pattern of the North Atlantic freshwater flux and versus the strength of the vertical mixing of heat and salt.

2. The global implicit ocean model

The global model here extends the model of [15] by applying the equations below to a global domain with the inclusion of realistic bathymetry, wind forcing and thermohaline forcing. The ocean velocities in eastward and northward directions are indicated by u and v, the vertical velocity is indicated by w, the pressure by p and the potential temperature and salinity by T and S, respectively. The governing equations in coordinates (λ, ϕ, z) are

$$\frac{\mathrm{D}u}{\mathrm{d}t} - \frac{uv\tan\phi}{r_0} - 2\Omega v\sin\phi = -\frac{1}{\rho_0 r_0\cos\phi}\frac{\partial p}{\partial\lambda} + Q_\tau^\lambda + \mathscr{F}^u, \tag{1a}$$

$$\frac{\mathrm{D}v}{\mathrm{d}t} + \frac{u^2\tan\phi}{r_0} + 2\Omega u\sin\phi = -\frac{1}{\rho_0 r_0}\frac{\partial p}{\partial\phi} + Q_\tau^\phi + \mathscr{F}^v, \tag{1b}$$

$$\frac{\partial p}{\partial z} = -\rho g, \tag{1c}$$

$$0 = \frac{\partial w}{\partial z} + \frac{1}{r_0\cos\phi}\left(\frac{\partial u}{\partial\lambda} + \frac{\partial(v\cos\phi)}{\partial\phi}\right), \tag{1d}$$

$$\frac{\mathrm{D}T}{\mathrm{d}t} = \nabla_h(K_\mathrm{H}\nabla_h T) + \frac{\partial}{\partial z}\left(K_\mathrm{V}\frac{\partial T}{\partial z}\right) + Q_T, \tag{1e}$$

$$\frac{\mathrm{D}S}{\mathrm{d}t} = \nabla_h(K_\mathrm{H}\nabla_h S) + \frac{\partial}{\partial z}\left(K_\mathrm{V}\frac{\partial S}{\partial z}\right) + Q_S, \tag{1f}$$

$$\rho = \rho(T, S) \tag{1g}$$

with

$$\frac{\mathrm{D}F}{\mathrm{d}t} = \frac{\partial F}{\partial t} + \frac{u}{r_0\cos\phi}\frac{\partial F}{\partial\lambda} + \frac{v}{r_0}\frac{\partial F}{\partial\phi} + w\frac{\partial F}{\partial z},$$

$$\nabla_h F = \left(\frac{1}{r_0\cos\phi}\frac{\partial F}{\partial\lambda}, \frac{1}{r_0}\frac{\partial F}{\partial\phi}\right)^\mathrm{T},$$

$$\nabla_h\cdot\mathbf{F} = \frac{1}{r_0\cos\phi}\frac{\partial}{\partial\lambda}F^\lambda + \frac{1}{r_0\cos\phi}\frac{\partial}{\partial\phi}(F^\phi\cos\phi),$$

where F, $\mathbf{F} = (F^{\lambda}, F^{\phi})^{\mathrm{T}}$ are an arbitrary scalar and vector, respectively and the superscript T indicates transpose.

In the equations above, vertical and horizontal mixing of heat and salt is represented by eddy diffusivities, with constant horizontal and vertical diffusivities K_{H} and K_{V} for both heat and salt. Laplacian friction is taken for the mixing of momentum (for the terms (F^{u},F^{v}), see [15]) with constant mixing coefficients A_{H} and A_{V} in the horizontal and vertical, respectively. Density ρ is related to potential temperature and salinity through an equation of state that is based on the polynomial expression used by [16]

$$\rho(T,S) = \rho_0\left[1 + a_1 S - b_1 T - b_2 T^2 + b_3 T^3\right]. \tag{2}$$

The ocean circulation is driven by a wind stress $\vec{\tau}(\lambda,\phi) = \tau_0(\tau^{\lambda},\tau^{\phi})^{\mathrm{T}}$, where τ_0 is the amplitude, and where $\tau^{\lambda}(\lambda,\phi)$ and $\tau^{\phi}(\lambda,\phi)$ provide the spatial patterns of the zonal and meridional winds. The transfer of momentum from the surface downwards occurs in a thin boundary layer, i.e., the Ekman layer. Although this may be explicitly resolved [17], we follow the methodology applied in many low-resolution ocean general circulation models. The surface forcing is distributed as a body forcing over a certain depth of the upper ocean using a vertical profile function $g(z)$

$$Q_{\tau}^{\lambda} = g(z)\frac{\tau_0}{\rho_0 H_m}\tau^{\lambda}, \quad Q_{\tau}^{\phi} = g(z)\frac{\tau_0}{\rho_0 H_m}\tau^{\phi}, \tag{3a}$$

where H_m is a typical vertical scale of variation of the profile function $g(z)$. The function $g(z)$ is taken unity in the upper layer and zero below, so that H_m is the depth of the surface ocean layer.

The upper ocean is coupled to a simple energy-balance atmospheric model, in which only the heat transport is modelled (no moisture transport). The atmospheric model used is one of the simplest versions within the class of energy-balance models [18]. The equation for the atmospheric surface temperature T_{a} on the global domain is given by

$$\begin{aligned}\rho_{\mathrm{a}} H_{\mathrm{a}} C_{pa}\frac{\partial T_{\mathrm{a}}}{\partial t} &= \rho_{\mathrm{a}} H_{\mathrm{a}} C_{pa} D_0 \nabla_h(D(\phi)\nabla_h T_{\mathrm{a}}) - (A + BT_{\mathrm{a}}) \\ &\quad + \frac{\Sigma_0}{4}S(\phi)(1-\alpha)(1-C_0) + \mu_{oa}(1-L)(T-T_{\mathrm{a}}) + \mu_{la}L(T_l - T_{\mathrm{a}}),\end{aligned} \tag{4}$$

where $\rho_{\mathrm{a}} = 1.25$ kg m^{-3} is the atmospheric density, $C_{pa} = 10^3$ J (kg K)$^{-1}$ the heat capacity, $\alpha = 0.3$ the constant albedo, $H_{\mathrm{a}} = 8.4 \times 10^3$ m an atmospheric scale height, $\Sigma_0 = 1.36 \times 10^3$ W m^{-2} the solar constant, $D_0 = 3.1 \times 10^6$ m^2 s^{-1} a constant eddy diffusivity and $1 - C_0 = 0.57$ is the atmospheric absorption coefficient. The functions $D(\phi)$ and $S(\phi)$ give the latitudinal dependence of the eddy diffusivity and the short-wave radiative heat flux with

$$D(\phi) = 0.9 + 1.5\exp\left(-\frac{12\phi^2}{\pi}\right), \quad S(\phi) = 1 - \frac{1}{2}(0.482(3\sin\phi)^2 - 1). \tag{5}$$

The constants $A = 216$ W m^{-2} and $B = 1.5$ W m^{-2}K^{-1} control the magnitude of the long-wave radiative flux.

In (4), T is the sea-surface temperature, T_l the temperature of the land surface points and the coefficient L indicates whether the underlying surface is ocean ($L = 0$) or land ($L = 1$). The exchange of heat between atmosphere and ocean and between atmosphere and the land surface is modelled by constant exchange coefficients. We assume here for simplicity that both are equal, with

$$\mu_{la} = \mu_{oa} = \rho_{\mathrm{a}} C_{pa} C_{\mathrm{H}} \mid V_{\mathrm{a}} \mid \equiv \mu, \tag{6}$$

where $C_{\mathrm{H}} = 1.22 \times 10^{-3}$ and $\mid V_{\mathrm{a}} \mid = 8.5$ ms^{-1} is a mean atmospheric surface wind speed; it follows that $\mu \approx 13$ W m^{-2} K^{-1}.

Boundary conditions for the atmosphere are periodic in zonal direction and no-flux conditions at the north–south boundaries, i.e.

$$T_{\mathrm{a}}(\lambda = \lambda_W) = T_{\mathrm{a}}(\lambda = \lambda_E), \quad \frac{\partial T_{\mathrm{a}}}{\partial \lambda}(\lambda = \lambda_W) = \frac{\partial T_{\mathrm{a}}}{\partial \lambda}(\lambda = \lambda_E), \tag{7a}$$

$$\phi = -\phi_S, \phi_N : \frac{\partial T_{\mathrm{a}}}{\partial \phi} = 0. \tag{7b}$$

The net downward heat flux into the ocean and land is given by

$$Q_{oa} = \frac{\Sigma_0}{4} S(\phi)(1-\alpha)C_0 - \mu(T - T_{\mathrm{a}}), \tag{8a}$$

$$Q_{la} = \frac{\Sigma_0}{4} S(\phi)(1-\alpha)C_0 - \mu(T_l - T_{\mathrm{a}}). \tag{8b}$$

When the heat capacity of the land is assumed zero, then $Q_{la} = 0$ and the land temperature T_l is computed directly from

$$T_l = T_{\mathrm{a}} + \frac{\Sigma_0}{4\mu} S(\phi)(1-\alpha)C_0. \tag{9}$$

The freshwater flux is prescribed in each of the results below and indicated by an amplitude F_0 and a spatial pattern F_S. Hence, the expressions for Q_T in (1e) and Q_S in (1f) become

$$Q_T = g(z)\frac{Q_{oa}}{\rho_0 C_p H_m}, \tag{10a}$$

$$Q_S = g(z)\frac{F_0 F_S}{H_m} \tag{10b}$$

and this forcing is again represented as a body forcing over the upper layer. On the continental boundaries, no-slip conditions are prescribed and heat- and salt fluxes are zero. At the bottom of the ocean, both the heat and salt fluxes vanish and slip conditions are assumed.

Note that the model formulated here does not guarantee stably stratified solutions. As in all other large-scale ocean models the effect of small-scale convection, which occurs when the stratification is not statically stable, must be explicitly parameterized. Such a parameterization is usually referred to as 'convective adjustment'. Two parameterizations have been implemented in the implicit model: the locally-enhanced diffusion parameterization [19] and the Global Adjustment Procedure [20]. In the former method, the mixing coefficient is increased locally in regions of unstable stratification. The Global Adjustment Procedure generates a stably stratified solution by increasing vertical diffusivities in an iterative procedure that removes all static instabilities.

3. Numerical methods

The equations are discretized in space using a second-order control-volume discretization method on a staggered (Marker and Cell or Arakawa C-) grid, that places the p, T and S points in the center of a grid cell, and the u, v, and w points on its boundaries. The spatially discretized model equations can be written in the form

$$\mathbf{M}\frac{\mathrm{d}\mathbf{u}}{\mathrm{d}t} = \mathbf{F}(\mathbf{u}) = \mathbf{L}(\mathbf{u}) + \mathbf{N}(\mathbf{u},\mathbf{u}), \tag{11}$$

where the vector $\mathbf{u}$ contains the unknowns (u, v, w, p, T, S) at each grid point. The operators $\mathbf{M}$ and $\mathbf{L}$ are linear and $\mathbf{N}$ represents the nonlinear terms in the equations.

In an implicit formulation, a class of two-level schemes can be written as

$$\mathbf{M}\frac{\mathbf{u}^{n+1}-\mathbf{u}^{n}}{\Delta t} - \Theta\mathbf{F}(\mathbf{u}^{n+1}) - (1-\Theta)\mathbf{F}(\mathbf{u}^{n}) = 0 \tag{12}$$

using a time step Δt and a time index n. For $\Theta = 1$, this is the Backward Euler scheme and for $\Theta = 1/2$, it is the Crank–Nicholson scheme. For each scheme, a system of nonlinear algebraic equations of the form

$$\frac{1}{\Delta t}\mathbf{M}\mathbf{u}^{n+1} - \Theta\mathbf{F}(\mathbf{u}^{n+1}) = \frac{1}{\Delta t}\mathbf{M}\mathbf{u}^{n} + (1-\Theta)\mathbf{F}(\mathbf{u}^{n}) \tag{13}$$

has to be solved, which is done with the Newton–Raphson method. Steady states, if they exist, can be found for one set of parameters by integrating in time and taking the limit $t \to \infty$.

3.1. Continuation of steady states

It is often very efficient to directly solve for steady states as a function of parameters. For $\mathrm{d}\mathbf{u}/\mathrm{d}t = 0$, (11) reduces to

$$\mathbf{F}(\mathbf{u},\mathbf{p}) = 0. \tag{14}$$

Here the parameter dependence of the equations is made explicit through the p-dimensional vector of parameters $\mathbf{p}$ and hence $\mathbf{F}$ is a nonlinear mapping from $\mathbf{R}^{d+p} \to \mathbf{R}^{d}$. To determine branches of steady solutions of the equations (14) as one of the parameters, say μ, is varied, the pseudo-arclength method [21] is used. The branches $(\mathbf{u}(s), \mu(s))$ are parameterized by an 'arclength' parameter s. An additional equation is obtained by 'normalizing' the tangent

$$\dot{\mathbf{u}}_0^{\mathrm{T}}(\mathbf{u}-\mathbf{u}_0) + \dot{\mu}_0(\mu-\mu_0) - \Delta s = 0, \tag{15}$$

where $(\mathbf{u}_0, \mu_0)$ is an analytically known starting solution or a previously computed point on a particular branch and Δs is the step-length.

To solve the system of Eqs. (14) and (15) a predictor–corrector method is applied. The secant method and Newton method are used as predictor and corrector, respectively. During one Newton iteration, with iteration index k, linear systems of the form

$$J(\mathbf{u}^{k})\begin{pmatrix}\Delta\mathbf{u}^{k+1}\\ \Delta\mu^{k+1}\end{pmatrix} = \begin{pmatrix}\mathbf{r}^{k}\\ r_{d+1}^{k}\end{pmatrix} \tag{16}$$

have to be solved, where $\Delta\mathbf{u}^{k+1}$ and $\Delta\mu^{k+1}$ are the updates, respectively. The quantities $\mathbf{r}^{k}$ and r_{d+1}^{k} are derived from (14) and (15) and are given by

$$\mathbf{r}^{k} = -\mathbf{F}(\mathbf{u}^{k},\mu^{k}), \quad r_{d+1}^{k} = \Delta s - \dot{\mathbf{u}}_0^{\mathrm{T}}(\mathbf{u}^{k}-\mathbf{u}_0) + \dot{\mu}_0(\mu^{k}-\mu_0). \tag{17}$$

The $(d+1)\times(d+1)$ Jacobian matrix J of (14) and (15) along a branch is given by

$$J(\mathbf{u}) = \begin{bmatrix}\Phi & \mathbf{F}_{\mu}\\ \dot{\mathbf{u}}_0^{\mathrm{T}} & \dot{\mu}_0\end{bmatrix}, \tag{18}$$

where Φ is the matrix of derivatives of $\mathbf{F}$ with respect to $\mathbf{u}$ and $\mathbf{F}_\mu$ the derivative of $\mathbf{F}$ with respect to the parameter μ.

When a steady state $\bar{\mathbf{u}}$ is determined, the linear stability of the solution is investigated by considering the evolution of infinitesimally small perturbations $\tilde{\mathbf{u}}$ on $\bar{\mathbf{u}}$. Linearization of the evolution equations for $\tilde{\mathbf{u}}$ and a normal mode analysis lead to a generalized eigenvalue problem of the form

$$A_1\mathbf{x} = \sigma A_2\mathbf{x}, \tag{19}$$

where $A_1 = \Phi$ and $A_2 = -\mathbf{M}$ are in general nonsymmetric matrices and $\sigma = \sigma_r + i\sigma_i$ is the complex growth rate. In the particular model here, A_2 is a singular diagonal matrix because time derivatives are absent in the continuity equation and vertical momentum equation. We use here the Simultaneous Iteration Technique [22] to solve for the most dangerous modes (i.e. those closest to the imaginary axis); for details see [14].

3.2. Solution of nonlinear algebraic systems

Since the Newton method requires computation and inversion of the Jacobian J in (16) at each iterative step, alternative corrector procedures have been applied. The algorithms that have been implemented are the Newton–Chord method, the Shamanskii method and the Adaptive Shamanskii method [23]. The Newton–Chord method is a so-called parallel chords method that uses a Newton step as the first iteration; this means that $J(\mathbf{u}^k)$ is replaced by the fixed matrix $J(\mathbf{u}^0)$. This Jacobian is computed and inverted once per continuation step and this matrix is being used throughout the iterative procedure. The drawback of the resulting gain in computational efficiency is a deterioration in convergence behavior from quadratic to linear.

The Shamanskii method alternates one 'outer' iteration of the Newton method with l 'inner' iterations of the Newton–Chord method. Taking a few inner iterations after each Newton step reduces the number of outer iterations considerably and speeds up convergence, which may become super-linear under reasonable circumstances. This procedure may even become more efficient if l is determined during the iterative process, rather than chosen beforehand, resulting in the Adaptive Shamanskii method. In the present code, l is determined on the basis of the time needed for an outer (T_o) and an inner iteration (T_i), and the convergence constants of the (quadratic) Newton method (k_n) and the (linear) Newton–Chord method (k_nc). If $\epsilon_n = ||x_n - x||$ is the error of the nth approximation of x, then with the Newton method the next approximation will have an error close to $\epsilon_{n+1} = k_\mathrm{n}\epsilon_n^2$. The number of Newton–Chord iterations l needed to attain the same accuracy can be estimated from $\epsilon_{n+1} = (k_\mathrm{nc})^l\epsilon_n$, leading to

$$l = \log(k_\mathrm{n}\epsilon_n)/\log(k_\mathrm{nc}). \tag{20}$$

Now, as long as

$$k_\mathrm{nc} < \exp\left[\log(k_\mathrm{n}\epsilon_n)\cdot\frac{T_\mathrm{i}}{T_\mathrm{o}}\right] \tag{21}$$

it holds that $l \cdot T_\mathrm{i} < T_\mathrm{o}$, and then it is more efficient to perform Newton–Chord iterations.

Higher efficiency can be obtained when the step size Δs of the arclength parameter s is adjusted during the continuation process. On parts of the branches of steady states, the solutions will vary little and large steps can be taken. On other parts, for instance when a saddle-node bifurcation is encountered, small steps are necessary to follow the curve in parameter space. We implemented a step-size control algorithm [24] that adjusts the step size with a factor $\xi = N_\mathrm{opt}/N$, which depends on the number of iterations N needed in the last continuation step, and an optimum value N_opt, which depends on the method used. For the Newton method $N_\mathrm{opt} = 4$ is chosen, for the other methods $N_\mathrm{opt} = 7$. If the corrector method diverges or does not converge within $2N_\mathrm{opt}$ iterations, the continuation step is repeated with halved step size.

3.3. MRILU

During the solution process described in the previous subsection, linear systems have to be solved. For the ocean model, these systems are nonsymmetric, ill-conditioned and of large dimension (about 300,000). A tailored method has to be used to solve these systems efficiently. We use a solver which is called Matrix Renumbering Incomplete LU (MRILU). MRILU is a multilevel ILU factorization in which simultaneously the factorization and the (multilevel) ordering is constructed, based on the magnitude of the matrix entries. Used within a Krylov-subspace method an effective solver results [25]. For the ocean model it appeared to be beneficial to do only a few reduction steps and hence only a few levels are used. On the coarsest level, a drop tolerance ILU factorization is used. The ocean model equations constitute a coupled system of six partial differential equations and therefore we use a block variant of MRILU in which the diagonal is a block diagonal matrix with blocks of order six.

MRILU is not a black box solver and requires a small set of parameters to be tuned for each particular problem at hand. For a limited number of reduction steps, the most critical parameter is the drop tolerance in the ILU factorization of the last block which determines the amount of memory to be used by the preconditioner. The smaller the tolerance the larger the fill-in and the faster the convergence. It provides a trade-off between CPU and memory usage.

As was indicated in [15], the performance of MRILU can be improved by an *a priori scaling* of the matrix. The effect of scaling on MRILU can be easily illustrated by considering the matrix

$$\begin{bmatrix} 1 & \alpha \\ \beta & 0 \end{bmatrix},$$

in which the zero is mimicking the zero block arising for the pressure in the continuity equation of the incompressible Navier–Stokes equations. If α or β is smaller than the drop tolerance then the dropping of one of these causes the matrix to become singular, which is undesired. This can be avoided by scaling the equations and the unknowns such that α and β are both of magnitude 1. To obtain an efficient method, this type of imbalance should be avoided by applying the scaling.

In [15], the scaling was determined manually and had to be tuned for each configuration separately. A major improvement in the present version is an algorithm which determines the scaling adaptively. The scaling is based on the average diagonal block (of order six) of the matrix, which we call B below. Let a typical off-diagonal block be indicated by C and assume that the diagonal blocks in the matrix are well represented by B. Then our aim with the scaling is that elements in C that lead to small contributions in both $B^{-1}C$ and CB^{-1} are to be dropped. In order to avoid that one of the criteria is much more stringent than the other, we require that the extrema per row and column of the inverse of B are of equal size.

An example serves to demonstrate the steps in the scaling. A typical diagonal block in the Jacobian matrix of the ocean model equations is given by

$$B = \begin{bmatrix} 2.16 & -0.08 & 0 & -9.05 & 0 & 0 \\ 0.02 & 2.04 & 0 & -6.08 & 0 & 0 \\ 0 & 0 & 0 & -6.00 & -0.79 & 0.60 \\ 0.11 & 0.07 & 6.40 & 0 & 0 & 0 \\ -12.1 & -7.70 & -630. & 0 & 29.3 & 0 \\ -0.11 & -0.04 & -4.79 & 0 & 0 & 25.3 \end{bmatrix}$$

and its inverse is

$$H \equiv B^{-1} = 10^{-2} \begin{bmatrix} 45.2 & 1.02 & -69.2 & -183. & -1.87 & 1.64 \\ -1.19 & 48.5 & -47.3 & -125. & -1.28 & 1.12 \\ -0.76 & -0.55 & 1.71 & 20.1 & 0.05 & -0.04 \\ -0.25 & -0.18 & -16.1 & -42.5 & -0.43 & 0.38 \\ 1.93 & 1.38 & -4.31 & 325. & 3.30 & 0.10 \\ 0.05 & -0.02 & -0.05 & 2.82 & -0.00 & 3.95 \end{bmatrix}.$$

Note that the extremum in the fourth column (325.) is about one hundred times larger than the extremum in the fifth column (3.30), which is undesirable. In order to balance rows and columns an algorithm performing the following operations is applied to H

1. Multiply the first row and column by respective factors, the product being one, such that the scaled elements H_{14} and H_{41} become more balanced. We require that the ratio of the scaled H_{14} and H_{41} is the square root of that of the original ratio. Likewise for the second row and column.
2. By scaling the fourth row and column by the same factor the element H_{44} is made of the same magnitude as H_{11}.
3. The third row and column are scaled by the same factor such that the maximum of $|H_{43}|$ and $|H_{33}|$ is of the same magnitude as H_{11}. In practice, we anticipate here for diagonal blocks occurring in later stages of the elimination process by dividing this factor by two.
4. The fifth row and column are scaled such that simultaneously the magnitude of H_{45} is equal to that of H_{54} and H_{55} is equal to H_{11}. We refrain from this double criterion if $|H_{45}H_{54}| < 0.01|H_{44}H_{55}|$ and use a symmetric scaling to satisfy only the last criterion. Likewise for H_{46}, H_{64} and H_{66}.

Applying this algorithm gives the following scaled inverse

$$\hat{H} \equiv \hat{B}^{-1} = 10^{-2} \begin{bmatrix} 45.2 & 1.00 & -18.4 & -35.6 & -36.3 & 0.11 \\ -1.21 & 48.5 & -12.8 & -24.9 & -25.3 & 0.74 \\ -5.49 & -3.86 & 3.26 & 28.3 & 6.44 & -0.19 \\ -1.32 & -0.96 & -22.6 & -43.8 & -44.6 & 1.31 \\ 1.36 & 0.96 & -0.81 & 44.6 & 45.2 & 0.05 \\ 0.88 & -0.39 & -0.25 & 9.69 & -0.49 & 45.2 \end{bmatrix}.$$

The net effect of the scaling is that now the extrema in each row and corresponding column are of the same order of magnitude. In practice, we determine this scaling from the average diagonal block B, and apply it then to each block; this effectively provides a row and column scaling of the whole matrix. Note that the scaling algorithm defined above is still problem dependent but that the same idea can be employed in each case.

3.4. Remaining problems

In the implicit model defined here, there remain two fundamental problems which still have to be overcome. The first problem is a restriction on the value of the lateral friction coefficient A_{H} and the second problem is an efficient and robust implementation of a 'convective adjustment' algorithm.

Many explicit ocean models of 4° resolution use typical values of $A_{\mathrm{H}} = 2.5 \times 10^5\ \mathrm{m^2\ s^{-1}}$. If one considers the momentum equations in a single-hemispheric basin [15], this value is far too small to resolve the Ekman boundary layer near the eastern wall. This boundary layer has a thickness $(A_{\mathrm{H}}/f_0)^{1/2}$, where $f_0 = 2\Omega \sin \phi_0$ is the value of the Coriolis parameter at latitude ϕ_0. General numerical practice is to resolve these boundary layers, since otherwise wiggles are encountered.

In the MOM model, it turns out that the steady states that are found indeed display wiggles near the eastern boundary, but their amplitude remains small. When the implicit model is used to compute steady states with this value of A_{H}, the wiggles are seen in the whole solution. The great advantage of the B-grid in

the MOM model turns up here, as the discretization of the Coriolis terms provide difficulties on the C-grid [26] due to the presence of the 'velocity modes'. The problem is exacerbated in the implicit approach because the whole system of equations is solved simultaneously and there is no decoupling of barotropic and baroclinic modes.

It has been shown that the problems with the velocity modes disappear with sufficient horizontal resolution [26]. Hence we have not pursued any fixes, such as first-order discretization of the Coriolis terms near the boundaries. As the B-grid has severe disadvantages in that pressure points are decoupled (occurrence of so-called 'pressure modes'), it seems no option in the development of implicit models. In the results below, we therefore restrict to the C-grid case in which the value of A_H is such that the lateral Ekman boundary layers are resolved and lateral friction damps the velocity modes.

Convective adjustment is widely used in ocean models and is easily implemented in explicit models, but it turns out to be difficult to use in implicit models. The main difficulty are the nondifferentiable properties associated with on/off behavior depending on the local vertical density gradient. Local convective adjustment may lead to spurious equilibria [27,28] while the Global Adjustment Procedure [15] cannot be used in a continuation set-up; the latter procedure is also very expensive. In addition, the convective adjustment procedure introduces huge off-diagonal coefficients to the matrix Φ in (18) and severely degrades the efficiency of the preconditioners. Hence, convective processes are not represented in the results below.

The resulting solutions appear 'less realistic' than those of other ocean models with a comparable resolution. However, they are the most 'clean' solutions of the governing system of hydrostatic partial differential equations, in that boundary layers are well-resolved and no ad-hoc procedures for convection have been applied. Under these limitations of the model, there are still many interesting problems to study with it, because many phenomena do not depend qualitatively on the value of A_H and on convective adjustment. Two of these problems will be considered in the next section: the hysteresis behavior of the thermohaline circulation and the scaling relation between the Atlantic meridional overturning and the vertical mixing coefficient K_V.

4. Capabilities of the implicit model

We first choose specific forcing conditions in Section 4.1 and then determine a reference steady state by continuation. The bifurcation diagram due to changes in the freshwater flux pattern is presented in Section 4.2. In Section 4.3, results of transient implicit computations are shown, while parameter sensitivity of the reference solution is considered in Section 4.4.

4.1. The reference solution

The model domain represents the entire World Ocean, with the longitude λ ranging from 0° to 360° and the latitude ϕ from 85.5°S to 85.5°N, on a 96×38 grid. The grid has 12 levels in the vertical and is non-equidistant with the most upper (lowest) layer having a thickness of 50 m (1000 m), respectively. The bathymetry is derived from the ETOPO-10 data set, which is interpolated onto the model grid and smoothed. Standard values of the model parameters are listed in Table 1. The mixing coefficients of heat and salt are typical for low-resolution ocean models, while the value of A_H is much larger, for reasons discussed above.

Starting from the trivial state, at zero solar forcing, no freshwater flux and no wind-stress, first an equilibrium state is determined under the annual-mean wind stress as in [29], the analytical form of the solar forcing and the Levitus surface salinity distribution [30]. For the computation of the reference solution, a restoring time scale of 75 days is used for the Levitus surface salinity; properties of the reference steady state are plotted in Fig. 1.

Table 1
Standard values of parameters used in the numerical calculations

$2\Omega = 1.46 \times 10^{-4}$ (s^{-1})	$r_0 = 6.37 \times 10^{6}$ (m)
$\rho_0 = 1.0 \times 10^{3}$ (kg m^{-3})	$A_V = 1.0 \times 10^{-3}$ (m^2 s^{-1})
$K_H = 1.0 \times 10^{3}$ (m^2 s^{-1})	$K_V = 8.0 \times 10^{-5}$ (m^2 s^{-1})
$C_p = 4.2 \times 10^{3}$ (J kg^{-1} K^{-1})	$g = 9.8$ (m s^{-2})
$A_H = 1.6 \times 10^{7}$ (m^2 s^{-1})	$H_m = 50$ (m)
$a_1 = 7.6 \times 10^{-4}$ (–)	$b_1 = 5.6 \times 10^{-5}$ (K^{-1})
$b_2 = 6.3 \times 10^{-6}$ (K^{-2})	$b_3 = 3.7 \times 10^{-8}$ (K^{-3})

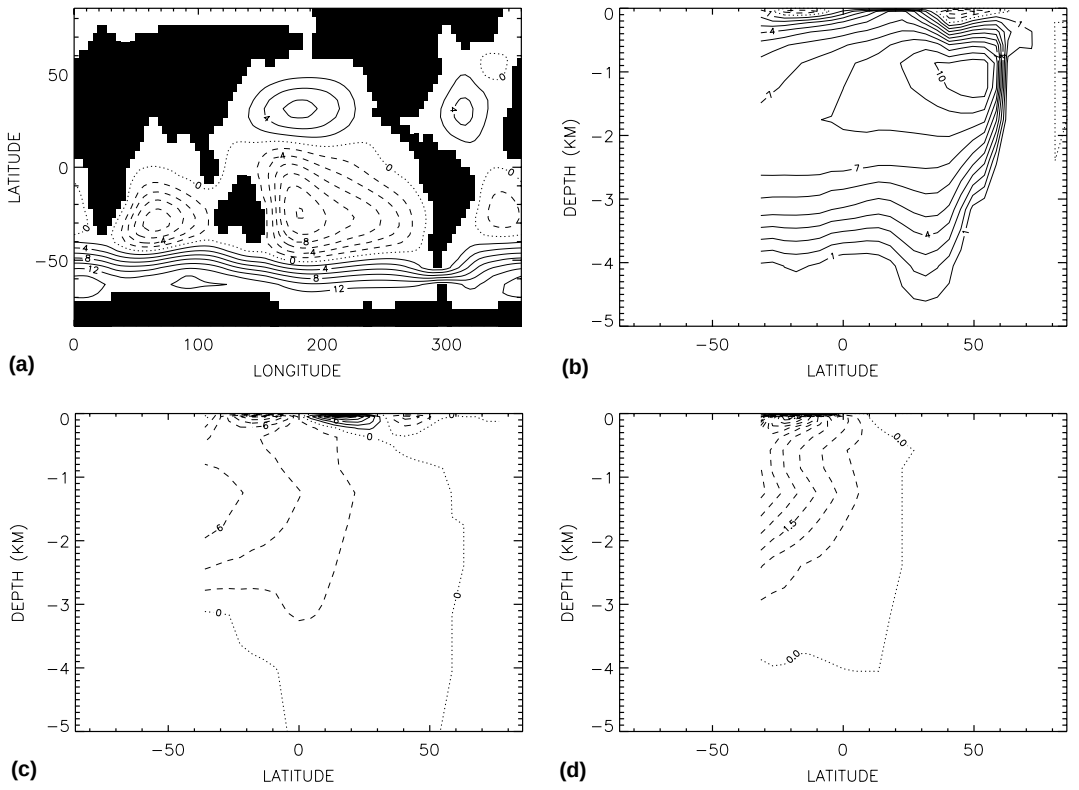

Fig. 1. Properties of the steady global ocean circulation pattern at standard parameter values and forcing conditions, with the surface salinity restored to Levitus values with a time scale of 75 days. Contour levels are in Sv. (a) Barotropic streamfunction ($\Psi_{min} = -15.8$ Sv, $\Psi_{max} = 12.1$ Sv), and (b–d) meridional overturning streamfunctions in the (b) Atlantic ($\Psi_{min} = -2.9$ Sv, $\Psi_{max} = 10.7$ Sv), (c) Pacific ($\Psi_{min} = -12.3$ Sv, $\Psi_{max} = 11.4$ Sv) and (d) Indian Ocean ($\Psi_{min} = -5.0$ Sv, $\Psi_{max} = 2.0$ Sv).

In the barotropic streamfunction (Fig. 1(a)), the Antarctic Circumpolar Current can be seen with the gyre structure in each basin. The maximum volume transport of the Antarctic Circumpolar Current is about 12 Sv – a factor 10 smaller than observed – the latter due to the large value of A_H. The maximum of the Atlantic meridional overturning streamfunction (Fig. 1(b)) is about 11 Sv, which is slightly smaller than in other models [31]; this is due to the absence of convective adjustment. As shown in [15], the difference between the unadjusted and adjusted solutions is usually a few Sv while the overall pattern of the overturning remains the same. There is also no bottom-water formation in the Southern Ocean and hence an equivalent of Antarctic Bottom Water is absent. The meridional overturning in the Pacific Ocean (Fig. 1(c))

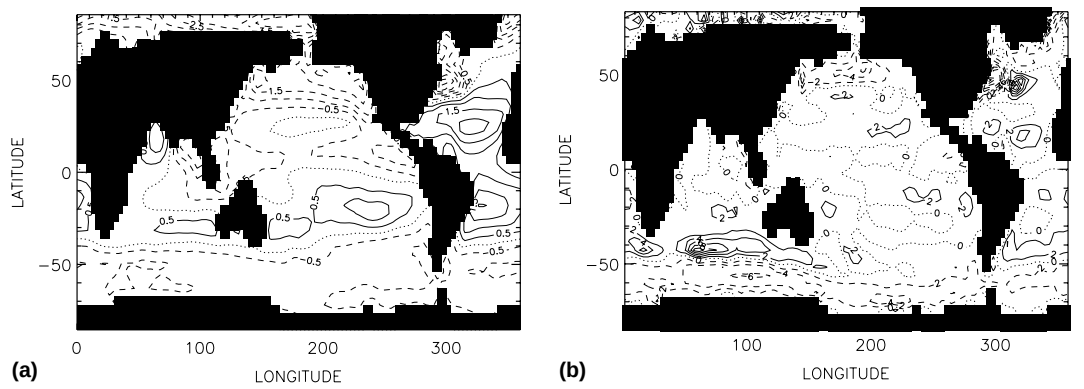

Fig. 2. (a) Surface salinity anomaly with respect to $S_0 = 35$ psu, with $S_{\min} = -4.7$ psu and $S_{\max} = 2.2$ psu. (b) Diagnosed freshwater flux field (in units of 10^{-8} ms^{-1}) of the state in Fig. 1. The minimum and maximum values are -15.8×10^{-8} m s^{-1} and 12.5×10^{-8} m s^{-1}, respectively.

and the Indian Ocean (Fig. 1(d)) is relatively strong with extremes of about −12 and −5 Sv, respectively. In all three oceans, there are Ekman driven surface circulation cells having a strength of a few Sv. Although many details of this equilibrium solution are incorrect when compared to observations, the overall characteristics of the global flow are captured.

Next, the freshwater flux is diagnosed from this reference solution; this flux (indicated by F_S^1, see Fig. 2(b)) is needed to maintain the Levitus surface salt field (shown in Fig. 2(a)) under the steady state reference flow. Largest amplitudes with typical values of 3.8 m yr^{-1} occur over the southern Indian Ocean and in the northern North Atlantic. Although the freshwater flux differs substantially from the observed annual mean field [32], there is reasonable agreement with the diagnosed fluxes calculated in other OGCMs [33,34]. For example, in the North Atlantic, there is a zonal dipolar structure with large amplitude that can also be seen in Fig. 8a of [34] and Fig. 2 of [33]. The salt input in the positive part of this dipole near 40° is needed to compensate for the model's incorrect representation of the salt transport due to the Gulf Stream.

4.2. The bifurcation diagram

We first define a region near New Foundland, similar to region A in [7], with domain $P = \{(\lambda, \phi) \in [300, 336] \times [54, 66]\}$. To study the impact of changes in the freshwater flux pattern, a perturbation flux F_{Sp} is defined as

$$F_{Sp} = \gamma_p F_S^2(\lambda, \phi) \tag{22}$$

where $F_S^2(\lambda, \phi) = 1$ in the region P and zero outside. The value of γ_p controls the amplitude of the freshwater perturbation and following previous model studies [7], it is expressed in Sv. When changing γ_p, one has to take care that the salt balance is closed, i.e. we subtract the surface integrated value Q from the total freshwater flux profile such that

$$\frac{1}{|S|}\int_S (F_S^1(\lambda, \phi) + \gamma_p F_S^2(\lambda, \phi)) r_0^2 \cos\phi \, \mathrm{d}\lambda \, \mathrm{d}\phi - Q = 0, \tag{23}$$

where $|S|$ is the total area of the ocean surface.

The bifurcation diagram, showing the maximum Atlantic meridional overturning Ψ_{atl} of the steady solutions versus γ_p, is plotted in Fig. 3. Drawn branches indicate linearly stable solutions, whereas the

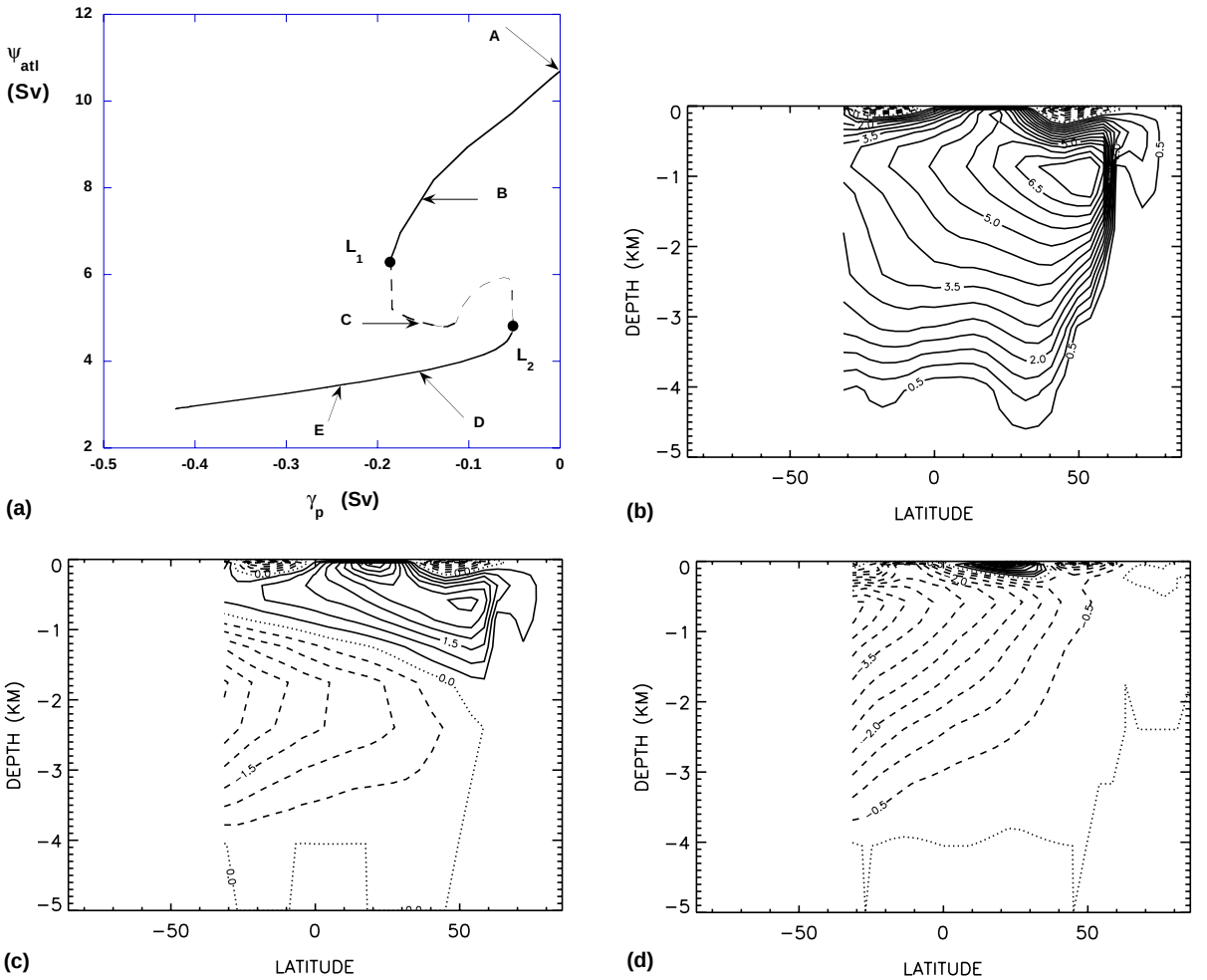

Fig. 3. (a) Bifurcation diagram showing the steady states of the global ocean circulation as a plot of the maximum meridional Atlantic overturning versus the anomalous freshwater-flux strength γ_p (in Sv). The point labelled A represents the reference solution (for $\gamma_p = 0$). (b) Pattern of the meridional streamfunction in the Atlantic for the state B in (a); contour values are in Sv, $\Psi_{\min} = -2.7$ Sv, $\Psi_{\max} = 6.4$ Sv; (c) Similar as (b) but for state C, $\Psi_{\min} = -3.9$ Sv, $\Psi_{\max} = 5.0$ Sv; (d) Similar as (b) but for state D, $\Psi_{\min} = -8.3$ Sv, $\Psi_{\max} = 2.9$ Sv.

solutions on the dashed branch are unstable. Complementary to the quasi-equilibrium simulations with OGCMs, the computations here provide: (i) the exact location of the saddle-node bifurcations (L_1 and L_2 in Fig. 3); and (ii) the solutions on the unstable branch. The saddle-node bifurcations (at $\gamma_p = -0.18$ Sv and $\gamma_p = -0.052$ Sv) exactly bound the regime of multiple equilibria of the global ocean circulation. For values of γ_p smaller than -0.18 Sv only the collapsed state exists.

The Atlantic meridional overturning streamfunction of the solutions at the locations B, C and D is plotted in Figs. 3(b)–(d), respectively. State B still has substantial northward sinking, while in state D northern sinking is absent. In the unstable state C, the northern sinking is substantially reduced but southern sinking is still relatively weak. Along the unstable (dashed) branch, the solution totally changes character as the northern sinking is inhibited and the volume of bottom water coming from the south increases. The Atlantic

overturning strength of the northern sinking solution seems to remain fairly constant along the unstable branch. However, this is a consequence of the norm chosen, since Ψ_{atl} is in this regime only determined by the wind-driven Ekman cell at the surface. For $\gamma_p = -0.23$ Sv, only the collapsed state E exists with a meridional overturning pattern similar to state D.

4.3. Transient flows

To illustrate the transient flows in this model, we focus on the case $\gamma_p = -0.15$. We take state B in Fig. 3 as the initial state and determine the flow behavior once an anomalous freshwater-flux forcing is applied to this state (over the domain P). Starting at state B, we change γ_p from -0.15 to -0.23 over a time interval $t \in (0, t_m]$. For $t > t_m$, the anomalous forcing is removed by switching γ_p back to -0.15. We monitor the evolution of the flow for different values of t_m using the implicit model. The bifurcation diagram in Fig. 3(a) indicates that state B may collapse to state D.

The drawn curve in Fig. 4 shows the evolution of the flow for $t_m = \infty$, i.e. a permanent freshwater-flux perturbation. In this case, the flow approaches the unique steady state for $\gamma_p = -0.23$ (which is state E in Fig. 3(a)) after about 1000 years. When $t_m = 100$ year, the Atlantic overturning circulation first decreases rapidly, but it recovers as soon as the forcing is removed. For large times, e.g. $t_m = 400$ year, the Atlantic overturning circulation collapses and it does not recover as the forcing is removed; the state D is finally approached. It turns out that the transition point separating recovery and collapse is located near $t_m = 220$ year for which the Atlantic overturning is about 5 Sv. The latter value is closely related to the value of the unstable state C.

In the initial stages of the flow evolution relatively small time steps have to be taken (0.2 year) for the Newton–Raphson process to converge. In the approach to steady state much larger time steps (up to 100 year) are possible. The transient computations were used to test the performance of the solver of the

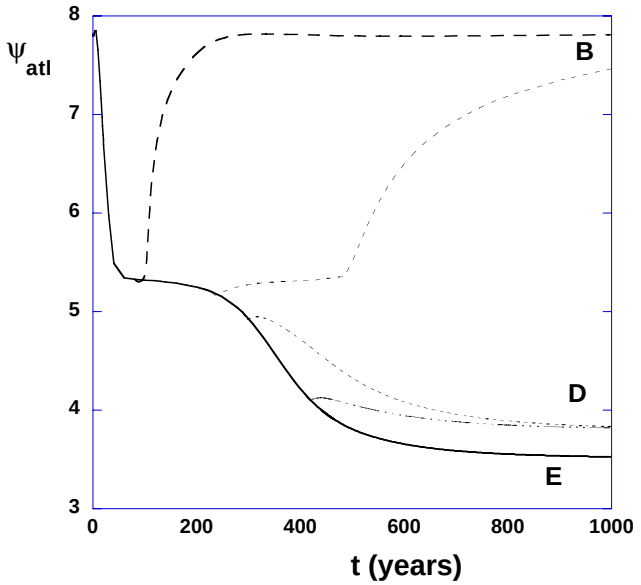

Fig. 4. Trajectories of the global model. The drawn curve starts at state B and shows the time evolution under conditions $\gamma_p = -0.23$ for $t_m = \infty$; it ends up for $t \to \infty$ in state E. The dashed curve is for $t_m = 100$ and the dash-dotted curve is for $t_m = 400$. The other two curves are for two times t_m just near the transition point separating recovery and collapse.

Table 2
CPU time and number of iterations for the test problem, for several time steps $\Delta t = 10$, 20 and 40 year, using the Newton–Raphson method and the Adaptive Shamanskii method. The residue in both methods is 1.0×10^{-6}. The timing is performed on a 500 MHz XP-1000 workstation with 2 Gb internal memory

Method	Δt (year)	# Decomp.	# It. steps	Time (s)
Newton–Raphson	10	3	3	1890
	20	4	4	3100
	40	4	4	3240
Adaptive Shamanskii	10	1	4	679
	20	1	5	778
	40	1	8	971

nonlinear system of equations. The case considered is for $t_m = \infty$ (the drawn curve in Fig. 4) at $t = 220$ year. Table 2 tabulates the total CPU time for one time step (10, 20 and 40 year) and the number of iterations taken, for both the Newton–Raphson and the Adaptive Shamanskii method described in Section 3.2. Note that a factor 3 reduction in CPU time can be achieved by applying the Adaptive Shamanskii method.

4.4. Parameter sensitivity

With the implicit model, the sensitivity of the solutions to parameters can be investigated efficiently. To illustrate this, we determined the dependence of the global flow versus the vertical mixing coefficient K_V. Starting at the reference solution and using restoring to the Levitus surface salt field (with a restoring time of 75 days), the steady states are followed in the parameter K_V. In Fig. 5, the Atlantic meridional overturning Ψ_{atl} is plotted versus K_V together with curves of different power law dependencies. Over the whole range of K_V, a clear 1/3 power dependence is found.

This result is interesting and stimulates further study. While there is much literature on these scaling relations in OGCM's for different configurations (e.g. [35]), there do not appear to be studies of the scaling of the global circulation. For thermohaline flows in a single-hemispheric basin, it has been well-established that the meridional overturning Ψ_M scales with K_V according to a 2/3 power dependence. This is in accordance with classical scaling arguments that do not consider the wind forcing [36], i.e. the 'thermal' wind balance, the continuity equation and an advection/diffusion balance of heat at the thermocline. These balances yield scales

$$\Psi_M \sim K_V^{2/3} r_0^{4/3} \left[\frac{\Delta \rho g}{2\Omega} \right]^{1/3}, \tag{24}$$

where $\Delta\rho$ is a characteristic meridional density difference.

One might think that the limitations of the model here (large A_H, no convective adjustment) would give a different scaling relation than those in single-hemispheric configurations. However, this is not the case. Using the implicit model, we computed the scaling relations for the single-hemispheric configuration as in [15], i.e. an ocean only model with a meridionally dependent idealized surface temperature forcing. In Fig. 6, the maximum meridional overturning Ψ_M^{max} is shown as a function of K_V for $A_H = 1.6 \times 10^7$ m^2 s^{-1} for both cases: without (Fig. 6(a)) and with (Fig. 6(b)) local convective adjustment. In agreement with previous model studies, a clear 2/3 power law dependence is found in both cases. We also used the MOM model with $A_H = 1.6 \times 10^5$ m^{2}s^{-1} and convective adjustment and found the same 2/3-power law [37].

These results indicate that the global scaling relations are indeed qualitatively different from the single-hemispheric case. A study by [38] has already indicated that this may occur due to the presence of the

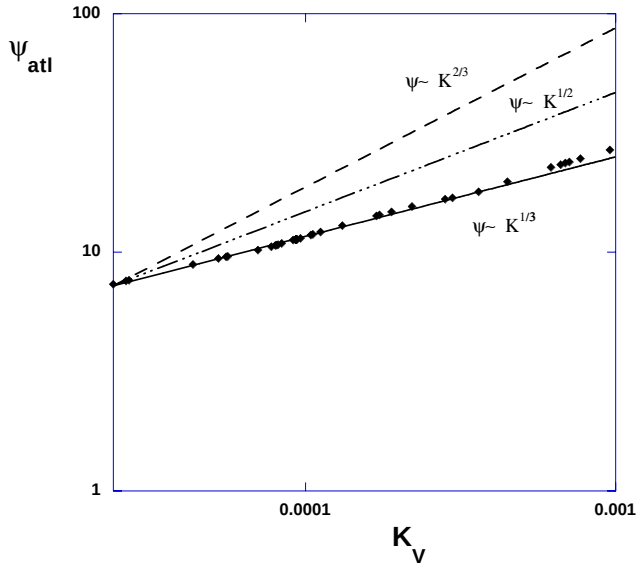

Fig. 5. Sensitivity of the Atlantic meridional overturning circulation (Ψ_{atl}) versus the vertical mixing coefficient K_V. Computed points with the arclength continuation are plotted as markers, while curves of (scaled) power law dependencies are also plotted (drawn 1/3, dashed 2/3, dash-dotted 1/2).

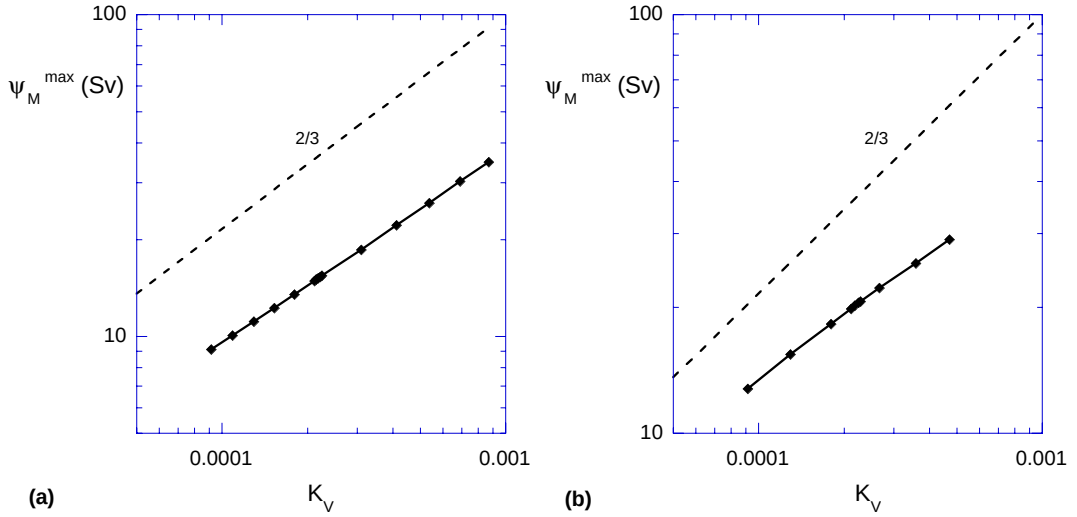

Fig. 6. Scaling behavior of the flow with K_V for the implicit model in the single-hemispheric configuration used in [15] for $A_H = 1.6 \times 10^7$ m^2 s^{-1} and (a) no-convective adjustment and (b) with convective adjustment.

Antarctic Circumpolar Current. The precise physical balances causing this behavior still have to be investigated and the explanation is outside the scope of this paper. Here, the result is only presented as a demonstration that arclength continuation with an implicit model is a highly efficient method to determine parameter sensitivities of model solutions.

5. Discussion and conclusion

As an alternative to traditional explicit ocean models, we have presented a fully-implicit formulation of the equations governing the ocean circulation in [15]. In the present paper, it is shown that this formulation can be applied to a global ocean configuration with realistic continental geometry and bathymetry. This new approach allows for a more efficient analysis of the sensitivity and stability of the global ocean circulation. We have demonstrated the potential of the model in following steady states through parameter space using continuation techniques and by performing time-integrations with very long time steps (relative to those in explicit models).

With the coarse resolution used, the model solutions capture only the overall large-scale properties of the global oceanic flow. For the solutions, the wind-driven circulation is severely underestimated because of the large value of A_{H}. Moreover, the strength of the meridional overturning is also underestimated because of the absence of convective adjustment. Although convective adjustment is not essential for generating thermohaline circulation, it is of quantitative importance for the strength of the overturning and the temperatures in the deep ocean [39,40]. In addition, improvements of the mixing parameterizations [41] are needed to increase the quality of the solutions.

With these clear limitations of the implicit model, we have demonstrated that still meaningful and interesting results can be obtained. The capabilities of the model were shown by computing the bifurcation diagram associated with the hysteresis behavior of the global circulation. As these transitions have been found in many low-resolution OGCMs in similar regimes of γ_p, the existence of the multiple equilibria regime appears not very sensitive to lateral friction and convective adjustment. The capabilities in computing trajectories using relatively large time steps has been demonstrated by looking at the evolution of the global circulation as it is temporarily perturbed with a freshwater-flux perturbation. The usefulness of the implicit model is here that one can efficiently compute the boundary between collapse and recovery. Finally, we found an interesting result in the scaling behavior of the global ocean circulation with the vertical mixing coefficient K_{V} by following steady states in parameter space.

The key to being able to perform these tasks is the solution of large linear systems of equations with tailored iterative solvers. The combination of the adaptively scaled MRILU preconditioning technique with a conjugate gradient solver [15] enables one to compute solutions to the steady or time-dependent equations for reasonable horizontal and vertical resolutions. While the present system (with a 4° horizontal resolution) contains over 280,000° of freedom, 2°-calculations with more than 1,000,000 degrees of freedom are currently in progress. As the performance of these solvers are still improving, it is not unreasonable to expect that solutions for a 1° resolution with about 5×10^6 degrees of freedom can be computed in the near future.

The results presented here open the way to address issues related to stability and variability of the global ocean circulation from a dynamical systems point of view [14]. The research tool presented here may therefore contribute to a fundamental understanding of the climate system and its low-frequency variability.

Acknowledgements

This work was supported by the Netherlands Organization for Scientific Research (NWO) under a PIONIER grant to H.D. The authors thank Jeroen Gerrits and Lianke te Raa (both at IMAU) for useful discussions and work on the scaling relations. All computations were performed on the SGI Origin 3800 at the Academic Computing Centre (SARA), Amsterdam, the Netherlands within the project SC029. Use of these computing facilities was sponsored by the National Computing Facilities Foundation with financial support from NWO.

References

[1] R.B. Alley, J. Marotzke, W.D. Nordhaus, J.T. Overpeck, D.M. Peteet, R.A. Pielke Jr., R.T. Pierrehumbert, P.B. Rhines, T.F. Stocker, L.D. Talley, J.M. Wallace, Abrupt climate change, Nature 299 (2003) 2005–2010.

[2] Y. Kushnir, Interdecadal variations in North Atlantic sea surface temperature and associated atmospheric conditions, J. Phys. Oceanogr. 7 (1994) 141–157.

[3] V. Moron, R. Vautard, M. Ghil, Trends, interdecadal and interannual oscillations in global sea-surace temperature, Clim. Dyn. 14 (1998) 545–569.

[4] T.L. Delworth, M.E. Mann, Observed and simulated multidecadal variability in the Northern hemisphere, Clim. Dyn. 16 (2000) 661–676.

[5] J.C. McWilliams, Modeling the ocean general circulation, Ann. Rev. Fluid Mech. 28 (1996) 215–248.

[6] R.C. Pacanowski, S.M. Griffies, MOM 3.0, User Manual GFDL/NOAA Report.

[7] S. Rahmstorf, Bifurcations of the Atlantic thermohaline circulation in response to changes in the hydrological cycle, Nature 378 (1995) 145–149.

[8] E.P. Chassignet, H. Arango, D. Dietrich, T. Ezer, M. Ghil, D.B. Haidvogel, C.-C. Ma, A. Mehra, A.M. Paiva, Z. Sirkes, DAMEE-NAB: the base experiments, Dyn. Atmos. Oceans 32 (2000) 155–183.

[9] K. Hasselmann, An ocean model for climate variability studies, Prog. Oceanogr. 11 (1982) 69–92.

[10] D.B. Haidvogel, A. Beckmann, Numerical Ocean Circulation Modelling, Imperial College Press, London, UK, 1999.

[11] S. Rahmstorf, The thermohaline circulation: a system with dangerous thresholds, Clim. Change 46 (2000) 247–256.

[12] H. Stommel, Thermohaline convection with two stable regimes of flow, Tellus 2 (1961) 230–244.

[13] M. Ghil, S. Childress, Topics in Geophysical Fluid Dynamics: Atmospheric Dynamics, Dynamo Theory, and Climate Dynamics, Springer-Verlag, Berlin/Heidelberg/New York, 1987.

[14] H.A. Dijkstra, Nonlinear Physical Oceanography: A Dynamical Systems Approach to the Large Scale Ocean Circulation and El Niño, Kluwer Academic Publishers, Dordrecht, The Netherlands, 2000.

[15] H.A. Dijkstra, H. Öksüzöglu, F.W. Wubs, E.F.F. Botta, A fully implicit model of the three-dimensional thermohaline ocean circulation, J. Comput. Phys. 173 (2001) 685–715.

[16] M. Winton, E.S. Sarachik, Thermohaline oscillations induced by strong steady salinity forcing of ocean general circulation models, J. Phys. Oceanogr. 23 (1993) 1389–1410.

[17] W.G. Large, J.C. McWilliams, S.C. Doney, Ocean vertical mixing: a review and a model with a nonlocal boundary layer parameterization, Rev. Geophys. 32 (1994) 363–403.

[18] G.R. North, R.F. Cahalan, J.A. Coakley, Energy balance climate models, Rev. Geophys. Space Phys. 19 (1981) 19–121.

[19] L.A. Te Raa, H.A. Dijkstra, Instability of the thermohaline ocean circulation on interdecadal time scales, J. Phys. Oceanogr. 32 (2002) 138–160.

[20] W. Weijer, H.A. Dijkstra, Bifurcations of the three-dimensional thermohaline circulation: the double hemispheric case, J. Mar. Res. 59 (2001) 599–631.

[21] H.B. Keller, Numerical solution of bifurcation and nonlinear eigenvalue problems, in: P.H. Rabinowitz (Ed.), Applications of Bifurcation Theory, Academic Press, New York, USA, 1977.

[22] W.J. Steward, A. Jennings, A simultaneous iteration algorithm for real matrices, ACM Trans. Math. Software 7 (1981) 184–198.

[23] C. Brezinski, Projection Methods for Systems of Equations, North-Holland Publishing Co., Amsterdam, 1997.

[24] R. Seydel, Practical Bifurcation and Stability Analysis: From Equilibrium to Chaos, Springer-Verlag, New York, USA, 1994.

[25] E.F.F. Botta, F.W. Wubs, MRILU: An effective algebraic multi-level ILU-preconditioner for sparse matrices, SIAM J. Matrix Anal. Appl. 20 (1999) 1007–1026.

[26] A. Adcroft, C.N. Hill, J.C. Marshall, A new treatment of the Coriolis terms in C-grid models at both high and low resolutions, Month. Weather Rev. 127 (1999) 1928–1936.

[27] M. Vellinga, Multiple equilibria of the thermohaline circulation as a side effect of convective adjustment, J. Phys. Oceanogr. 28 (1998) 305–319.

[28] N.R. Edwards, J.G. Shepherd, Multiple thermohaline states due to variable diffusivity in a hierarchy of models, Ocean Modeling 3 (2001) 67–94.

[29] K.E. Trenberth, J.G. Olson, W.G. Large, A global ocean wind stress climatology based on ECMWF analyses, Tech. rep., National Center for Atmospheric Research, Boulder, CO, U.S.A., 1989.

[30] S. Levitus, R. Burgett, T. Boyer, World Ocean Atlas 1994, Volume 3: Salinity., NOAA Atlas NESDIS 3, US Department of Commerce, Washington DC, 1994, 0-99.

[31] M.H. England, Representing the global-scale water masses in ocean general circulations models, J. Phys. Oceanogr. 23 (1993) 1523–1552.

[32] J.M. Oberhuber, The Budget of Heat, Buoyancy and Turbulent Kinetic Energy at the Surface of the Global Ocean, Max Planck Institute fur Meteorologie Hamburg report nr. 15, Hamburg, Germany, 1988.

[33] E. Tziperman, J.R. Toggweiler, Y. Feliks, K. Bryan, Instability of the thermohaline circulation with respect to mixed boundary conditions: Is it really a problem for realistic models?, J. Phys. Oceanogr. 24 (1994) 217–232.
[34] A.J. Weaver, T.M. Hughes, On the incompatibility of ocean and atmosphere and the need for ux adjustments, Clim. Dyn. 12 (1996) 141–170.
[35] F. Bryan, Parameter sensivity of primitive equation ocean general circulation models, J. Phys. Oceanogr. 17 (1987) 970–985.
[36] P. Welander, The thermocline problem, Phil. Trans. Roy. Soc. London A 270 (1971) 415–421.
[37] L.A. Te Raa, Internal variability of the thermohaline ocean circulation, Ph.D. Thesis, Utrecht University, Utrecht, The Netherlands, 2003.
[38] A. Gnanadesikan, A simple predictive model of the structure of the oceanic pycnocline, Science 283 (1999) 2077–2081.
[39] J. Marotzke, P. Welander, J. Willebrand, Instability and multiple steady states in a meridional-plane model of thermohaline circulation, Tellus 40 (1988) 162–172.
[40] J. Marotzke, J.R. Scott, Convective mixing and the thermohaline circulation, J. Phys. Oceanogr. 29 (1999) 2962–2970.
[41] P.R. Gent, J. Willebrand, T.J. McDougall, J.C. McWilliams, Parameterizing eddy-induced tracer transports in ocean circulation models, J. Phys. Oceanogr. 25 (1995) 463–474.